Laboratory measurements and theoretical calculations of O_2 A band electric quadrupole transitions

D. A. Long,[1] D. K. Havey,[2] M. Okumura,[1] H. M. Pickett,[3] C. E. Miller,[3] and J. T. Hodges[2]

[1]*Division of Chemistry and Chemical Engineering, California Institute of Technology, Pasadena, California 91125, USA*

[2]*Process Measurements Division, National Institute of Standards and Technology,*
100 Bureau Drive, Gaithersburg, Maryland 20899, USA

[3]*Jet Propulsion Laboratory, California Institute of Technology, 4800 Oak Grove Drive, Pasadena, California 91109, USA*

Frequency-stabilized cavity ring-down spectroscopy was utilized to measure electric quadrupole transitions within the $^{16}O_2$ A band, $b\,^1\Sigma_g^+ \leftarrow X\,^3\Sigma_g^-(0,0)$. We report quantitative measurements (relative uncertainties in intensity measurements from 4.4% to 11%) of nine ultraweak transitions in the ^NO, ^PO, ^RS, and ^TS branches with line intensities ranging from 3×10^{-30} to 2×10^{-29} cm molec.$^{-1}$. A thorough discussion of relevant noise sources and uncertainties in this experiment and other cw-cavity ring-down spectrometers is given. For short-term averaging ($t < 100$ s), we estimate a noise-equivalent absorption of 2.5×10^{-10} cm^{-1} Hz$^{-1/2}$. The detection limit was reduced further by co-adding up to 100 spectra to yield a minimum detectable absorption coefficient equal to 1.8×10^{-11} cm^{-1}, corresponding to a line intensity of $\sim 2.5 \times 10^{-31}$ cm molec.$^{-1}$. We discuss calculations of electric quadrupole line positions based on a simultaneous fit of the ground and upper electronic state energies which have uncertainties <3 MHz, and we present calculations of electric quadrupole matrix elements and line intensities. The electric quadrupole line intensity calculations and measurements agreed on average to 5%, which is comparable to our average experimental uncertainty. The calculated electric quadrupole band intensity was $1.8(1) \times 10^{-27}$ cm molec.$^{-1}$ which is equal to only $\sim 8 \times 10^{-6}$ of the magnetic dipole band intensity.

PACS number(s): 33.70.Fd, 33.70.Ca

I. INTRODUCTION

In 1961, Noxon observed the first electric quadrupole transitions of molecular oxygen in the (subsequently named) Noxon band $a\,^1\Delta_g \leftarrow b\,^1\Sigma_g^+$ [1]. In 1981, electric quadrupole transitions within the electronic ground state of O_2 were identified by Goldman *et al.* [2] in the solar spectra of Niple *et al.* [3] and observed in the laboratory spectra of Reid *et al.* [4]. Quadrupole transitions within the O_2 A band, $b\,^1\Sigma_g^+ \leftarrow X\,^3\Sigma_g^-(0,0)$, were observed in the solar spectra of Brault [5]. Brault was able to produce line positions and intensities for eight transitions ($N'' = 5$ to 19) within the ^TS branch of the $^{16}O_2$ A band. See Sec. II for notation. The only laboratory observation of an electric quadrupole line within the O_2 A band was performed by Naus *et al.* who measured the $^TS(9)$ line with a signal-to-noise ratio (SNR) of $\sim 2:1$ using pulsed cavity ring-down spectroscopy (CRDS) [6].

The O_2 A band is of special significance due to its extensive use over the past 50 years in remote sensing of the Earth's atmosphere. Measurements of this band have the potential to yield surface pressures to 0.1% [7] and enable accurate CO_2 remote sensing ($\sim 0.3\%$) by constraining surface pressure and photon path length in these retrievals. Use of the O_2 A band has been expanded in recent years to ground-based observations of solar spectra such as those of the TC-CON network [8]. Also, solar absorption by this band is used in satellite sensing of atmospheric gases by the GOME [9], SCIAMACHY [10,11], GOSAT [12] missions and was to be used in the OCO [13–15] mission.

Although the electric quadrupole transitions of the A band are 10^5 times weaker than the corresponding magnetic dipole transitions, they can be observed in atmospheric spectra [5,16] reaching 1% absorbance at high solar zenith angles. Failure to include electric quadrupole absorptions in O_2 A band remote sensing retrievals will lead to systematic errors in the assessment of photon path lengths, cloud or aerosol optical depths, and atmospheric pressure at the scattering height [7]. The situation is compounded since many of the electric quadrupole transitions occur underneath the much stronger magnetic dipole transitions. For these same reasons, the failure to include electric quadrupole transitions in fits of the line shape and line mixing parametrizations of the magnetic dipole transitions may result in systematic errors in the representation of the magnetic dipole features.

We present quantitative laboratory-based CRDS measurements which constitute observations of ultraweak (line intensities ranging from 3×10^{-30} to 2×10^{-29} cm molec.$^{-1}$) electric quadrupole transitions in the ^NO, ^PO, ^RS, and ^TS branches of the O_2 A band. We note that Brault [5] measured isolated ^TS lines which lie above the R-branch bandhead. Figure 1 shows the calculated positions and intensities of the four electric quadrupole (and magnetic dipole) branches, where the electric quadrupole intensities are based on the transition matrix elements described in Sec. IV C. The ^TS lines are relatively easy to observe in comparison with detection of ^NO, ^PO, and ^RS lines that are nearly degenerate with the magnetic dipole transitions—as are reported in the present study. We also discuss pertinent short- and long-time noise sources in this, and other, cw-CRDS experiments. Line intensities are assigned and combined (absolute) uncertainties in line intensity are estimated by evaluating random and systematic measurement uncertainties. Finally, we present theoretical calculations of line intensities and positions and compare these predictions to our experimental results.
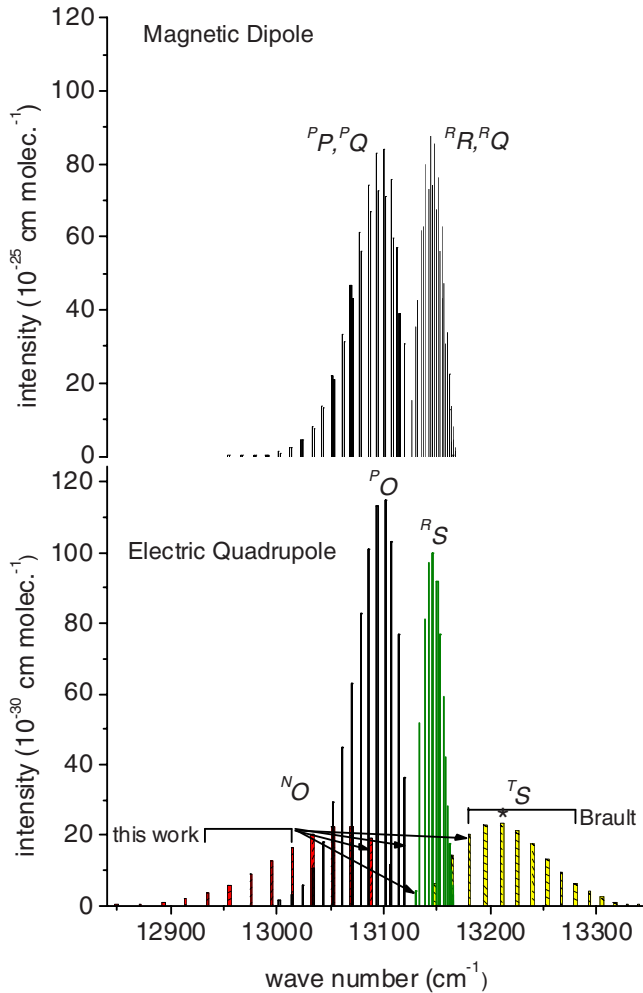
FIG. 1. (Color online) Stick spectra of magnetic dipole (upper panel) and electric quadrupole (lower panel) $^{16}O_2$ A band line intensities at $T=296$ K. Positions for the electric quadrupole lines are given in Table II. Transitions from the present study and those of Brault [5] as indicated. The symbol $*$ indicates the transition observed by Naus *et al.* [6]. Note the difference in scales of the vertical axes.

II. BACKGROUND

The O_2 A band, with a band origin at wave number $\tilde{\nu}$ $=13\ 122$ cm^{-1}($\lambda=762$ nm), is the strongest near-infrared absorption feature in the Earth's atmosphere. Although the transition is triply forbidden by quantum mechanical electric dipole selection rules (*gerade-gerade*, singlet-triplet, and Σ^+-Σ^-), magnetic dipole and electric quadrupole transitions are allowed [17,18]. The magnetic dipole transitions are 10^7 times weaker than a typical electric dipole transition and the electric quadrupole transitions are a further 10^5 times weaker (see Sec. IV C 2) than the magnetic dipole transitions.

The rotational energy levels of molecular oxygen are described by three quantum numbers: N, the rotational angular momentum, S, the spin angular momentum, and J, the total angular momentum ($J=N+S$). We therefore, describe the A band transitions by $^{\Delta N}\Delta J(N'')$, where the double prime indicates the lower state. An energy level diagram for the O_2 A band is shown in Fig. 2, illustrating that there are three J
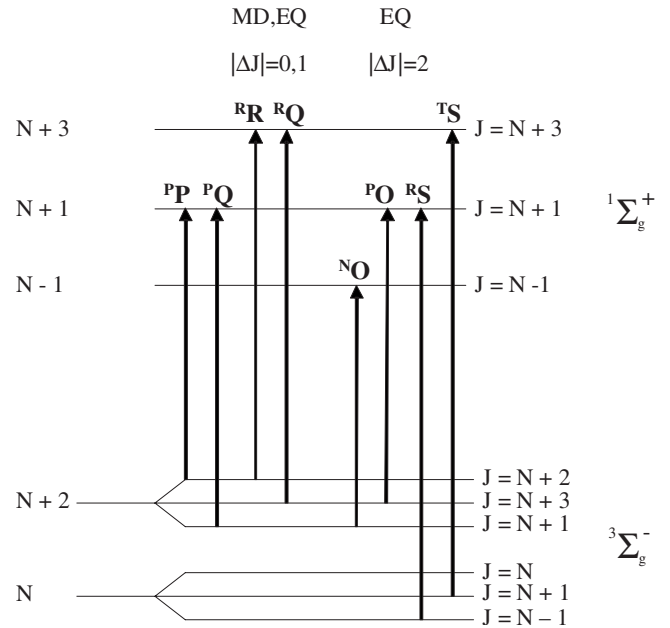

FIG. 2. Energy level diagram of molecular oxygen (only for $^{16}O_2$ and $^{18}O_2$) for the $X\ ^3\Sigma_g^-$ ground state and the $b\ ^1\Sigma_g^+$ excited state. The $|\Delta J|=0,1$ branches ($^PP,^PQ,^RR,^RQ$) are shown on the left for ground state rotational angular momentum, N (odd), and total angular momentum, J. These branches are both magnetic dipole (MD) and electric quadrupole (EQ) symmetry allowed. Similarly, on the right four symmetry-allowed electric quadrupole transition branches measured in this work are shown ($^PO,^NO,^RS,^TS$).

levels for every N in the triplet ground state. For even values of N (in the case of $^{16}O_2$ and $^{18}O_2$) the spin-statistical weight is 0 and hence only odd N are allowed. The ^PP, ^PQ, ^RR, and ^RQ branches, corresponding to $|\Delta J|=0,1$ are both magnetic dipole and electric quadrupole allowed. Given the weakness of the electric quadrupole transition moments, we do not expect them to contribute significantly to line intensities in the $|\Delta J|=0,1$ branches. The $|\Delta J|=2$ electric quadrupole transitions correspond to four branches: ^NO, ^PO, ^RS, and ^TS. The ^TS and ^NO branches have $|\Delta N|=3$, whereas the ^PO and ^RS branches have $|\Delta N|=1$. As can be seen in Fig. 1, these two $|\Delta N|=1$ branches are heavily masked by the P and R branches of the magnetic dipole transitions, respectively, with line positions differing, on average, by only 0.2 to 0.3 cm^{-1}. Only the $N''=1$ transition for each of these two branches is isolated from its sister magnetic dipole transition and can therefore be feasibly measured in this laboratory experiment.

Line position calculations

The positions of the electric quadrupole transitions were calculated based on a simultaneous fit of the ground $X\ ^3\Sigma_g^-$ and upper $b\ ^1\Sigma_g^+$ states using SPFIT [19]. Microwave [20–23], far-infrared [24], and Raman [25–28] positions for the $v=0$ and $v=1$ levels of the ground state were taken from the literature and used with their reported uncertainties. The A band positions reported by Robichaud *et al.* [29] yielded parameters for the upper state and also improved the distor-

TABLE I. Spectroscopic constants (cm^{-1}) of the $X\,^3\Sigma_g^-$ and $b\,^1\Sigma_g^+$ states of $^{16}O_2$. Lower state energy levels are defined in Ref. [25] and those of the upper state are given by $v_0 + B_0 J(J+1) - D_0 J^2(J+1)^2 + H_0 J^3(J+1)^3$. Numbers in parentheses represent 1σ uncertainty in units of the least significant digit.

$X\,^3\Sigma_g^-$ state	This work	Rouillé *et al.* [25]
B_0	1.437676078(29)	1.437676476(77)
D_0	$4.84178(14) \times 10^{-6}$	$4.84256(63) \times 10^{-6}$
H_0	$4.28(19) \times 10^{-12}$	$2.80(16) \times 10^{-12}$
λ_0	1.98475118(5)	1.984751322(72)
λ_0'	$1.9470(3) \times 10^{-6}$	$1.94521(50) \times 10^{-6}$
λ_0''	$9.70(3) \times 10^{-12}$	$1.103(41) \times 10^{-11}$
μ_0	$-8.4253696(58) \times 10^{-3}$	$-8.425390(13) \times 10^{-3}$
μ_0'	$-8.136(22) \times 10^{-9}$	$-8.106(32) \times 10^{-9}$
μ_0''	$-4.04(15) \times 10^{-14}$	$-4.70(19) \times 10^{-14}$
$b\,^1\Sigma_g^+$ state	This work	Robichaud *et al.* [29]
v_0	13122.0057456(89)	13122.00575(1)
B_0	1.39124922(11)	1.3912496(1)
D_0	$5.36909(28) \times 10^{-6}$	$5.3699(3) \times 10^{-6}$
H_0	$1.65(33) \times 10^{-14}$	$-1.80(2) \times 10^{-12}$

TABLE II. Calculated vacuum wave numbers (cm^{-1}) for the electric quadrupole transitions within the ^NO, ^PO, ^RS, and ^TS branches of the $^{16}O_2$ A band using our lower and upper state rotational parameters given in Table I. Transitions probed in this study are underlined. We use the designation $^{\Delta N}\Delta J(N'')$, such that $^NO(13)$ indicates the $[(N'=10) \leftarrow (N''=13),\ (J'=12) \leftarrow (J''=14)]$ transition.

N''	^NO	^PO	^RS	^TS
1		13119.92145	13130.35305	13147.74429
3	13105.75288	13113.96544	13133.57572	13164.04113
5	13088.15293	13107.60461	13138.22862	13179.92388
7	13070.22159	13100.86413	13142.54086	13195.41358
9	13051.93672	13093.75012	13146.48617	13210.51223
11	13033.29479	13086.26481	13150.05690	13225.21793
13	13014.29577	13078.40910	13153.24888	13239.52744
15	12994.94055	13070.18320	13156.05889	13253.43688
17	12975.23027	13061.58694	13158.48395	13266.94194
19	12955.16606	13052.61982	13160.52106	13280.03801
21	12934.74895	13043.28109	13162.16713	13292.72019
23	12913.97982	13033.56974	13163.41892	13304.98336
25	12892.85936	13023.48451	13164.27298	13316.82215
27	12871.38808	13013.02394	13164.72571	13328.23096
29	12849.56627	13002.18633	13164.77328	13339.20396

tion constants for the ground state compared to fits using only the ground state transitions. The final fit included 327 transitions and yielded a reduced root-mean-square (rms) uncertainty of 0.843, indicating that the relative weighting of the experimental data was slightly conservative. Note that we switched assignments for the $(N', J' \leftarrow N'', J'') = (11, 11 \leftarrow 13, 13)$ and $(11, 10 \leftarrow 13, 12)$ transitions at $\tilde{\nu} = 1482.4971$ cm^{-1} and 1482.4739 cm^{-1}, respectively, compared to the assignments reported by Brodersen and Bendtsen [27]. This resulted in a 62% reduction in the reduced rms of the total ground-state-only fit. Our fitted parameters for both lower and upper states as well as those of Rouillé *et al.* [25] (lower state) and Robichaud *et al.* [29] (upper state) are given in Table I, and our predicted electric quadrupole positions are given in Table II. Uncertainties in our predicted positions of the electric quadrupole transitions are predicted to be less than 3 MHz (10^{-4} cm^{-1}) since these transitions are based on the same energy levels as the magnetic dipole transitions (Fig. 2) [29].

However, when we compare our calculated positions to the calculations of Naus *et al.* [6], we find that their positions are systematically $\sim$300 MHz(0.01 cm^{-1}) lower than ours for both the magnetic dipole and electric quadrupole transitions. We believe that pressure shifting is the root of this discrepancy. Our line positions were calculated based upon laboratory measurements which have been corrected for pressure shifting, while no such correction was applied to the solar observations of Brault [5] and Babcock *et al.* [17] which formed the basis for the Naus *et al.* calculations. Brown and co-workers [30] have previously noted a similar discrepancy between the magnetic dipole line positions of several high-resolution laboratory studies [30–32] and those of Babcock *et al.* The direction and magnitude of the observed shift is consistent with the reported pressure shifting

of Robichaud *et al.* [33] (~ -0.002 MHz Pa^{-1} or -0.007 cm^{-1} atm^{-1}) for the P-branch of the A band magnetic dipole transitions. Thus, we believe that the calculations of Naus *et al.* [6] would agree with ours if the former were corrected for atmospheric pressure shifting. Additionally, the value reported by Naus *et al.* for the $^RS(1)$ line position is approximately 1 cm^{-1} low compared to both our reported value and our recalculation of this position using their specified spectroscopic constants.

As described below, having accurate knowledge of the line positions (i.e., those given in Table II) facilitated our efforts to unambiguously locate the electric quadrupole lines. This information, combined with accurate measurements of probe laser frequency, made it sufficient to interrogate the absorption spectrum over narrow spectral ranges centered on each expected line position.

III. EXPERIMENT

All measurements were made at the National Institute of Standards and Technology (NIST), in Gaithersburg, Maryland using the frequency-stabilized cavity ring-down spectroscopy (FS-CRDS) technique. This technique, which enables precise and accurate measurements of both the absorption coefficient and spectrum frequency axis, has been described previously [34,35]. See Fig. 3(a) for a schematic of the setup. The fundamental distinction between FS-CRDS and traditional cw-CRDS is that the cavity length is actively locked through the use of a co-resonant reference laser beam. In addition, the probe beam frequency is selectively locked to longitudinal modes of the TEM$_{00}$ cavity mode.
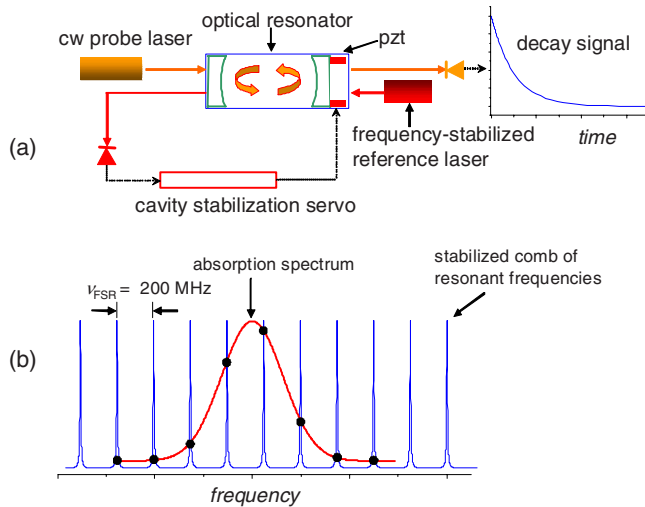
FIG. 3. (Color online) Experimental configuration. (a) Principal components of the frequency-stabilized cavity ring-down spectrometer, including probe and reference lasers, ring-down cavity, and length-stabilization servo. (b) Spectral acquisition scheme illustrating how the probe laser is scanned over successive longitudinal modes of the resonant cavity. The equally spaced modes are separated by ~200 MHz and form a frequency axis whose long-term precision is limited by the stability of the reference laser. With this approach, the absorption spectrum is discretely sampled at fixed intervals as indicated by the solid circles.

A. Experimental apparatus

The reference laser was a frequency-stabilized HeNe laser ($\lambda = 633$ nm) with a long-term (8 h time interval) frequency variation less than 2 MHz and output power of 1 mW. The probe beam was from a continuous-wave external-cavity diode laser (ECDL) with a Litmann-Metcalf resonator configuration. A Faraday isolator (−40 dB of isolation) was mounted directly on the probe laser housing. The ECDL output was single-mode and had a typical output power of 6–10 mW over the wavelength range $\lambda = 759-771$ nm. We used custom-made, dichroic ring-down cavity mirrors with nominal transmission losses of 3×10^{-5} and 0.05 at $\lambda = 765$ nm and 633 nm, respectively. Losses at the probe wavelength corresponded to a cavity finesse, $\mathcal{F} \sim 105\,000$, and the cavity length was 74 cm, yielding an effective optical path length of ~25 km. The mirror losses were ~7 times smaller compared to those of our previous FS-CRDS O_2 A band studies [29,36]. However, the short-term detection limit (discussed below) was only ~4 times lower than previously demonstrated because of reduced signal intensity of the decay signals.

The internal volume of the ring-down cavity was ~0.2 l, and all internal surfaces (except for Cu gaskets used in vacuum-compatible knife-edge seals) were made of electropolished stainless steel. We performed all experiments at room temperature and made no effort to control the temperature of the ring-down cell. The sample temperature, T, was measured using a NIST-calibrated 2.4 kΩ thermistor mounted in good thermal contact with an external wall of the ring-down cavity. Uncertainty in the measured sample temperature was limited by temperature gradients within the

cavity and was estimated to be less than 0.2 K. Cell wall temperature varied by at most 0.2 K during the course of a day, and the average temperature for all spectra was 295.25 K ± 0.3 K. All measurements were made on O_2 with >99.9% purity and natural isotopic abundance. We measured gas pressure, p, using two NIST-calibrated capacitance diaphragm gauges with full-scale responses of 13.3 and 133 kPa, respectively. We estimated the relative combined standard uncertainty in the pressure measurement to be less than 0.2% of the reading over the entire pressure range.

Spectra were acquired by locking the probe laser frequency to successive longitudinal modes of the frequency-stabilized ring-down cavity as shown in Fig. 3(b). As was previously demonstrated [29,33], this approach provides an exceptionally linear spectrum frequency axis with a step size given by, ν_{FSR}, where FSR is the cavity free-spectral range. The spectral resolution was limited by the stability of the HeNe reference laser. To measure absolute frequencies and the cavity FSR, we used a commercial Michelson-interferometer wave meter having a precision of 30 MHz ($\Delta \tilde{\nu} = 0.001$ cm^{-1}). We determined the mean cavity FSR to be 202.569(15) MHz by measuring the frequency steps of nearly 1000 spectra, each spanning a range of 10 GHz. The 15 kHz uncertainty in FSR is due to variations in the effective path length of the ring-down cavity caused by concomitant changes in the sample index of refraction as the pressure was varied between 2.5 and 30 kPa. The wave meter was calibrated against the measured position of the $^P P(11)$ $^{16}O^{18}O$ A band magnetic dipole transition. This line is within 0.15 cm^{-1} of the $^N O(5)$ electric quadrupole line, and its position was recently determined with an uncertainty of 4×10^{-5} cm^{-1} through the FS-CRDS method [37] by using hyperfine components of the D_1 and D_2 lines of ^{39}K as an absolute frequency reference [29].

We used a variable-frequency (200 MHz ± 10 MHz) acousto-optic modulator (AOM) to provide a first-order diffracted beam that was mode matched into the ring-down cavity. A Si-PIN photoreceiver (bandwidth of 700 kHz and responsivity of 0.3 V W^{-1}) located at the cavity output measured probe beam transmission. Ring-down decay events were initiated by transmission bursts having amplitudes exceeding an adjustable threshold. These bursts triggered TTL pulses from a digital delay generator, switching off the AOM power (decay time <50 ns) and shifting the AOM frequency by 10 MHz. The resulting ring-down signals were digitized by a 12-bit analog-to-digital board at a rate of 25 M samples/s and had maximum decay times of 80 μs. The decays were acquired at a nominal acquisition rate, f_{acq} =10 Hz. To obtain the decay time constant, τ, we fitted an exponential decay plus a dc baseline to each signal using the algorithm of Halmer *et al.* [38].

Spectra could be continuously measured over a 24 h interval without operator intervention. We employed two modes of laser tuning (coarse and fine). Coarse tuning was performed through the use of a stepper-motor-actuated grating (9 GHz minimum movement), while fine tuning was done via a piezoelectric (PZT)-actuated mirror (full range of 60 GHz). The stepper motor, PZT, and wave meter were automatically used in combination to move the laser frequency to the desired starting point for an individual scan.

Once this location was found, the PZT was employed to step the laser frequency over successive cavity longitudinal modes, q_m. A typical scan spanned a total of ~ 10 GHz, and took roughly ten to fifteen minutes. 50 individual ring-down time constants were averaged at each frequency step. The spectrum frequency axis was given by $\Delta q_m \nu_{FSR}$ where Δq_m was the number of mode steps through which the laser was tuned relative to the beginning of the scan. At least ten complete spectra were then co-added to produce a final averaged spectrum. The effects of these two separate averaging steps will be explored in detail in the next two sections

B. Short-term measurement statistics and signal averaging

It is instructive to consider both short- and long-term averaging statistics to evaluate system performance and quantify detection limits and measurement precision. With regard to short times, we use the noise-equivalent absorption coefficient ϵ_{NEA} given by $\sigma_\tau/(c\bar{\tau}^2 f_{acq}^{1/2})$. Here σ_τ represents the standard deviation of the observed time constant about its mean value, $\bar{\tau}$, and c is the speed of light. For a given averaging time, Δt_{av}, (corresponding to a set of ring-down signals acquired at fixed laser frequency) the uncertainty in the mean value of the base loss, $\bar{\alpha}$, is $u(\bar{\alpha}) = \epsilon_{NEA}/(\Delta t_{av})^{1/2} = \sigma_\tau/(c\bar{\tau}^2 n_d^{1/2})$, where n_d is the total number of measured decay signals. We found that $\sigma_\tau/\bar{\tau}$ was typically less than 0.2%, leading to a $\epsilon_{NEA} = 2.5 \times 10^{-10}$ cm^{-1} Hz$^{-1/2}$. For the averaging time employed, $\Delta t_{av} = 5$ s, this corresponded to an uncertainty in the absorption coefficient of $\alpha_{min,acq} = 1.1 \times 10^{-10}$ cm^{-1}.

For sufficiently long averaging time scales, the noise-equivalent absorption coefficient cannot be used to predict detection limits because of slow drift in system variables. We observed that our system exhibited a nominally linear drift in $\bar{\tau}$ over a time span of several hours given by $\sigma_\tau^{-1} d\bar{\tau}/dt \sim 2 \times 10^{-5}$ s^{-1}. The Allan variance, which was originally formulated to quantify the performance of ultrastable clocks [39], provides a useful measure of long-term system stability and has been applied to analyze detection limits in laser absorption spectroscopy [40]. We measured the Allan variance under empty-cavity conditions. The results for our experiment are shown in Fig. 4 and reveal an optimal averaging time of 150 s. For averaging time scales smaller than 150 s, the Allan variance varied inversely with Δt_{av} consistent with the definition of ϵ_{NEA}, whereas for longer averaging time scales, the Allan variance reached a minimum due to system drifts. When evaluated at the optimum averaging time, the Allan variance analysis yields a minimum uncertainty in the absorption coefficient of $\alpha_{min} = 4 \times 10^{-11}$ cm^{-1}, which corresponds to the peak loss from a self-broadened A band line with an intensity $S \sim 6 \times 10^{-31}$ cm^{-1} molec.$^{-1}$ at $p = 13.3$ kPa (100 Torr). Numerical simulations indicate that the optimal averaging time in our Allan variance is consistent with our observed drift rate.

C. Long-term averaging of spectra

In addition to short-time averaging of successive ring-down time constants, ensembles of complete spectra were also averaged. It is important to note that this is a simple
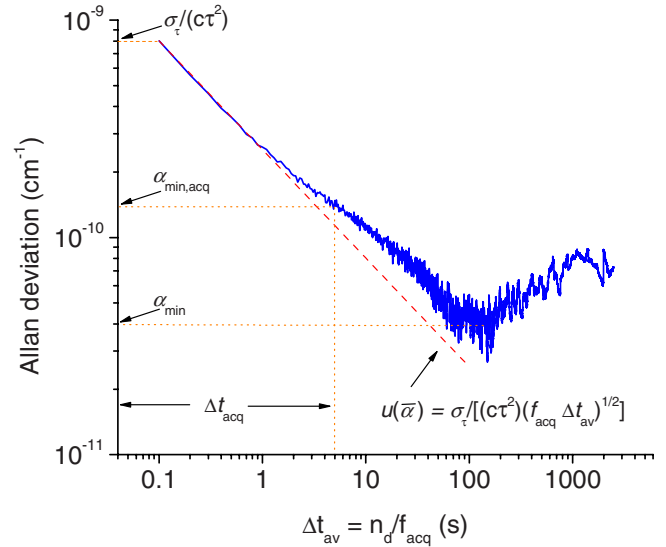

FIG. 4. (Color online) Measured Allan deviation (square root of the Allan variance) of the cavity losses as a function of averaging time, Δt_{av}. The quantity n_d is the number of measured decay signals, and the ring-down signal acquisition rate is f_{acq}. The dashed line tangent to the Allan deviation corresponds to $\epsilon_{NEA} = 2.5 \times 10^{-10}$ cm^{-1} Hz$^{-1/2}$ and for short averaging times gives an uncertainty in $\bar{\alpha}$, $u(\bar{\alpha})$, which is proportional to $n_d^{-1/2}$.

average; no baseline correction or other pre-analysis was performed. It was found that, over time, the broadband baseline absorbance drifted (as is to be expected due to thermomechanical drift); however, the integrated area of the relevant absorbance feature was independent of this drift. This is an important feature of FS-CRDS which allows spectra to be co-added, thereby reducing the amplitude of temporally uncorrelated residual features which vary on a time-scale shorter than our single-spectrum acquisition time (10–15 min).

The base losses of ring-down spectrometers typically have a weak wavelength dependence that drifts slowly with time. The baseline spectrum of the empty cavity arises from λ dependence in the mirror reflectivity and from secondary resonant cavities (etalons). Spectral and temporal variation in the base losses is a manifestation of coupling between cavities of low finesse and the main high-finesse ring-down cavity [41], and consequently the measured decay time τ is influenced by all resonant cavities along the optical axis of the probe beam. The most important secondary cavities are formed by pairs of surfaces where the first surface corresponds to one of the high-reflectivity ring-down cavity mirrors and the other corresponds to a normal-incidence surface in the probe beam path. Examples of the latter include: mode-matching lenses, view ports, detector faceplates, ring-down mirror input surfaces, etc. Note that a pair of coupled cavities will be mutually resonant at a given frequency, when the round-trip path difference is an integral multiple of $\lambda/2$. This effect gives rise to periodicity in the base losses as a function of optical frequency. Fourier analysis of ring-down spectra reveals the amplitudes and characteristic spatial frequencies (and hence path lengths) associated with these secondary resonators. Given that these etalons can involve op-
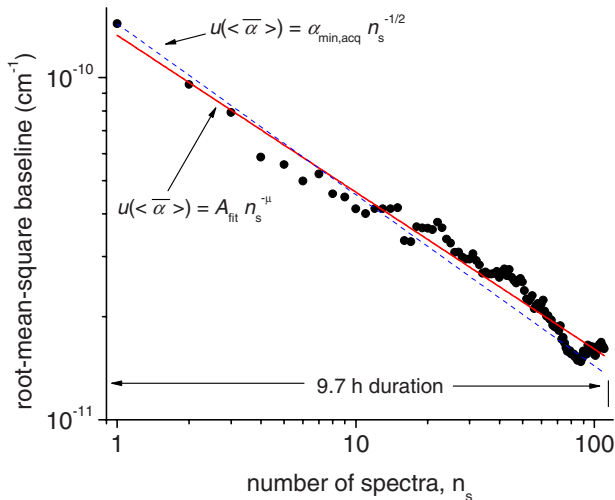
FIG. 5. (Color online) Decrease in rms baseline noise (symbols) with increasing number of co-added spectra, n_s. The solid red line corresponds to a power-law fit yielding the decay exponent, $\mu=0.46$ and the constant $A_{fit} \sim \alpha_{min,acq} = 1.1 \times 10^{-10}$ cm^{-1}. The dashed blue line represents an ergodic decay proportional to $n_s^{-1/2}$. The minimum value of the rms baseline corresponds to the peak loss of a self-broadened A band line with $S \sim 2.5 \times 10^{-31}$ cm^{-1} molec.$^{-1}$ at $p=13.3$ kPa (100 Torr).

tical elements external to the ring-down cavity, they are sensitive to slow thermomechanical variations in optical path length, therefore contributing to drift in the observed ring-down losses.

We evaluated the baseline noise of a composite spectrum by calculating the residuals to a quadratic fit in a region largely free of absorption features. The resulting rms baseline (in units of cm^{-1}) as a function of number of spectra averaged, n_s, can be found in Fig. 5. The overall trend is a steady reduction in the rms baseline noise to a minimum value of 1.8×10^{-11} cm^{-1}. This trend persists for an averaging time of approximately 10 h and shows no evidence of leveling off, indicating that additional gains could be achieved by further averaging. As shown in Fig. 5, a power-law fit to the data gives a slightly smaller decay exponent of $\mu=0.46$ than would be expected from an ergodic $n_s^{-1/2}$ dependence. Note the rms baseline for $n_s=1$ is consistent with the single-spectrum $\alpha_{min,acq}$ value shown in Fig. 4. Kassi *et al.* [42] similarly observed that co-adding cw-CRDS spectra reduced rms baseline noise in measurements made with a fibered distributed feedback (DFB) diode laser at 1.58 μm. However, they found a slightly faster decay of noise in their setup ($\mu=0.61$), which they assigned to the presence of slowly varying "interference fringes" whose movement was driven by thermomechanical drift.

D. Effect of long-term averaging on observed line shape

One possible deleterious result of spectra averaging is that the averaged spectrum may exhibit a nonphysical line shape due to instrumental broadening. To examine instrumental broadening, we measured the $^P P(21)$ transition of $^{16}O_2$ at $\tilde{\nu} = 13041.1236$ cm^{-1} both with and without the frequency sta-

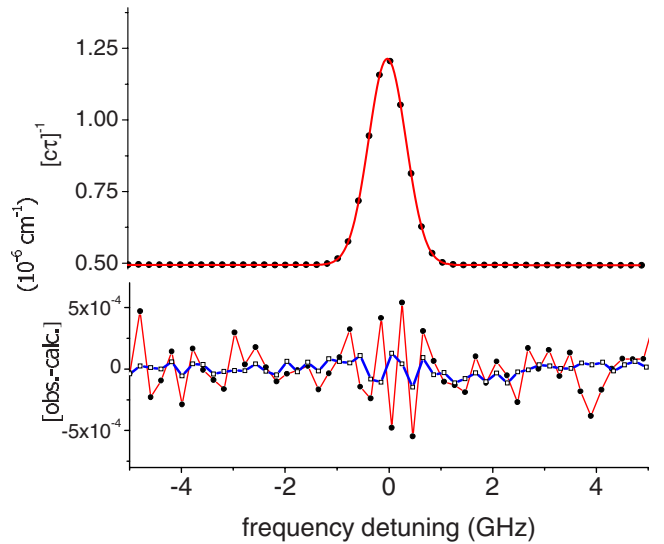

FIG. 6. (Color online) Frequency-stabilized, Doppler-broadened spectrum of the $^{16}O_2$ $^P P(21)$ magnetic dipole transition at $\tilde{\nu} = 13\,041.1236$ cm^{-1} for $p=67$ Pa, $T=294.987(40)$ K, and an effective pathlength of 25 km. Upper panel shows the measured (symbols) and Galatry line shape fit (solid line) to a single spectrum. Lower panel shows the fit residuals for the single spectrum, and those corresponding to the fit of an averaged spectrum comprising 28 spectra (blue line with open symbols). SNR for the averaged spectrum was 18,000:1 with rms noise in the baseline absorption coefficient of 3.9×10^{-11} cm^{-1}.

bilization at $p=67$ Pa. At this pressure the line shape was essentially Doppler broadened. The frequency-stabilized case is shown in Fig. 6. A Galatry profile [43] was fit to the measured spectra to account for residual pressure broadening as well as collisional narrowing effects that were observable at the high SNR of these measurements. We used the recent line shape measurements of Robichaud *et al.* [36] for the broadening and narrowing coefficients of this line, which were 0.0118 MHz Pa^{-1} and 0.0039 MHz Pa^{-1}, respectively.

We observed significant differences between the stabilized and unstabilized spectra with respect to the measured Doppler width and center frequency determinations. In the stabilized case, the mean difference between the measured Doppler width and the calculated value (~ 0.85 GHz) was 143 kHz, with a standard deviation of 329 kHz. In the unstabilized case, the difference was three times larger (379 kHz) and the measured standard deviation was six times larger (1.96 MHz). Apparent drifts in the transition center frequency as large as ~ 2 MHz min^{-1} were observed which resulted from continuous movement of the cavity modes over the 10 min duration of each spectrum acquisition. These effects of cavity drift were mitigated in the stabilized case, for which we measured a standard deviation in fit-derived center frequency of only 200 kHz. The residual scatter in center frequency for the stabilized case was driven in part by variations (occurring on the time scale of spectrum acquisition) in the HeNe laser reference frequency.

These results illustrate that with frequency stabilization of the ring-down cavity, the measured Doppler width and center frequency are stable to within 0.5 MHz. Therefore, co-

adding multiple spectra obtained over time spans of several hours should introduce negligible instrumental broadening in the present experiment. We conclude that our measurements of the weak electric quadrupole lines, obtained by co-adding multiple spectra, can be readily modeled using standard line shapes [44].

E. Analysis of measured spectra

Higher-order line shape phenomena such as collisional narrowing [43] and speed-dependent effects [45] were not expected to be detectable for measurements of the ultraweak electric quadrupole lines. Therefore, we modeled all these lines as Voigt profiles. The observed spectra, given by the measured quantity $n_0(c\tau)^{-1}$, comprised absorption by O_2 and all other system losses. Here n_0 is the broadband (nonresonant) index of refraction of the cavity medium, which we assumed to be unity. The electric quadrupole lines were superimposed on a baseline (linear plus sinusoidal terms) to capture variations in the local loss arising from wings of other lines and etaloning effects. The spectrum frequency axis was $\nu(q_{\mathrm{m}}) = \nu_0 + q_{\mathrm{m}}\nu_{\mathrm{FSR}}$, where ν_0 was the starting frequency given by the wave meter. The electric quadrupole line intensities are given by $S = \mathcal{A}/(nc)$, where $\mathcal{A}$ is the fitted area of the electric quadrupole peak, and n is the measured sample number density equal to $p(k_{\mathrm{B}}T)^{-1}$, in which k_{B} is the Boltzmann constant. The Gaussian width, w_{G}, was calculated in terms of the measured temperature, transition frequency, and $^{16}O_2$ molecular mass. For the lines considered here, w_{G}, expressed as a full width at half-maximum (FWHM), was nominally 0.85 GHz.

Given the relatively low SNR of the electric quadrupole spectra, it was not possible to retrieve the Lorentzian width, w_{L}, from the fitting procedure with sufficient accuracy. Instead, we constrained w_{L} to be $2\gamma p$, where γ is the pressure broadening coefficient. This constraint also ensured self-consistency in the fit-derived areas for a given line as the sample pressure was varied. We used the empirical J-dependent correlation of Yang *et al.* [46] with the parameters found in the self-broadening measurements of O_2 A band magnetic dipole P-branch spectra of Robichaud *et al.* [36] to calculate γ as

$$\gamma = A + \frac{B}{1 + c_1 J' + c_2 J'^2 + c_3 J'^4}, \tag{1}$$

where J' is the upper state angular momentum, $A = 0.004\,481$ MHz Pa^{-1}, $B = 0.012\,69$ MHz Pa^{-1}, and c_1, c_2, and c_3 equal 0.03723, -7.86×10^{-4}, and 1.05×10^{-6}, respectively. Note that these parameters are presently utilized to calculate the broadening coefficients found in HITRAN 2008 [47].

To test the applicability of Eq. (1), we relaxed the above constraint on w_{L} and subsequently retrieved γ from fits to the spectra. Figure 7 shows the results of these measured γ values and the predicted J'-dependent widths given by Eq. (1). Although the spread in the measurements is relatively large compared to the predicted variation with J', the mean γ values derived from the fits agrees well with the above correlation. The effect of uncertainty in γ on the uncertainty of the measured line intensities will be addressed in the Sec. IV B.
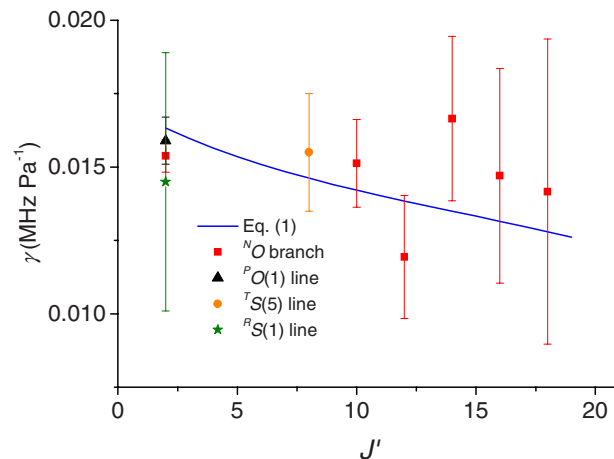

FIG. 7. (Color online) Measured (filled symbols) and calculated (line) self-broadening coefficient, γ, vs J'.

IV. RESULTS AND DISCUSSION

A. Electric quadrupole line intensity measurements

We used FS-CRDS to measure six electric quadrupole transitions in the ^{N}O branch and one transition each in the ^{P}O, ^{R}S, and ^{T}S branches of the O_2 A band. Except for the $^{T}S(5)$ transition, none of these transitions has previously been detected. We found good agreement between our observed and calculated line positions, with a mean deviation within the standard uncertainty of our calibrated frequency reference (60 MHz or 0.002 cm^{-1}).

As discussed in the Experiment section, 50 ring-down acquisitions were averaged per frequency step within an individual spectrum. At least ten complete spectra were then co-added to produce a final averaged spectrum. The effect of the reduction in baseline noise level achieved by co-adding electric quadrupole spectra can be seen in Fig. 8. It is apparent that a feature, which is only arguably observable in a single
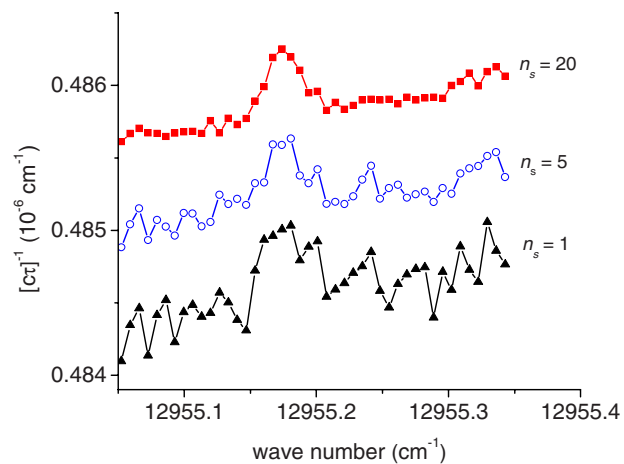

FIG. 8. (Color online) Increase in SNR of average absorption spectrum with increasing number of averaged spectra. Central peak corresponds to the $^{N}O(19)$ electric quadrupole transition of $^{16}O_2$($\tilde{\nu} = 12\,955.1661$ cm^{-1}, $S = 6.36 \times 10^{-30}$ cm molec.$^{-1}$) at $p = 12.7$ kPa. The middle and top spectra are offset in the vertical direction by 0.0005 and 0.0010 units, respectively.
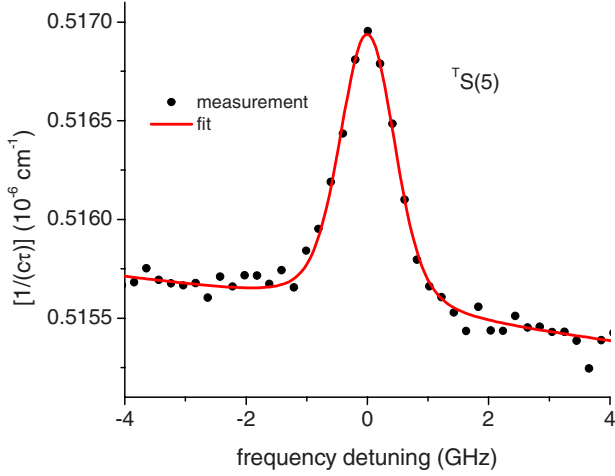
FIG. 9. (Color online) $^TS(5)$ electric quadrupole line of $^{16}O_2(\tilde{\nu} = 13\ 179.9239\ \mathrm{cm}^{-1})$ at $p = 12.7$ kPa, $T = 299.4$ K. Symbols represent measured values and the line is a fit based on the Voigt line shape. The measurements correspond to the average of ten scans, giving a SNR > 50:1.

scan given the high noise level, is clearly visible with a SNR 10:1 after averaging twenty scans. Figure 9 shows the relatively isolated $^TS(5)$ transition, which was previously measured by Brault [5] and which we readily measured with a SNR > 50:1.

The reduction in noise with signal averaging allows the quantitative observation of ultraweak absorption features within the wings of much stronger lines. The benefits of signal averaging are illustrated in Fig. 10, which shows an average of 23 individual spectra, for the $^NO(21)$ electric quadrupole transition. This is the weakest line probed in the present study. Nevertheless, it can clearly be seen in the wings of a $^{16}O_2$ hot band line. The absorption peak of the electric quadrupole line is 3.4×10^{-10} cm^{-1} and the rms baseline is 2.1×10^{-11} cm^{-1}, giving a peak SNR of 16:1.

Averaged spectra were acquired at several pressures between 3.33 and 26.7 kPa, with each spectrum yielding a measurement of line intensity. The mean line intensity for each transition (see Table III) was obtained by a weighted average over all measurements taken at various pressures. We used a normalized weighting factor proportional to $(n_j + \varepsilon_j^{-2})^{1/2}$, where n_j is the number of co-added spectra comprising the jth measurement, and $\varepsilon_j(p_j)$ is the fractional uncertainty in the jth measurement arising from systematic error in γ (as discussed below). We observed linearity between peak area, $\mathcal{A}_i$, and O_2 number density, n, for all measured transitions. This result is illustrated in Fig. 11, where the solid lines intersecting the origin correspond to the calculated peak areas based on the mean line intensity for each case (i.e., $\mathcal{A}_{i,\mathrm{calc}} = n\langle S_i \rangle c$).

For completeness, the measured intensities were also corrected to the standard reference temperature $T_r = 296$ K using the relation,

$$S(T_r) = S(T) \frac{Q(T)}{Q(T_r)} \frac{e^{-hcE''/(k_B T_r)}}{e^{-hcE''/(k_B T)}}, \qquad (2)$$

where E'' is the lower state energy, and $Q(T)$ is the total partition function for $^{16}O_2$. Lower state energies for the mea-
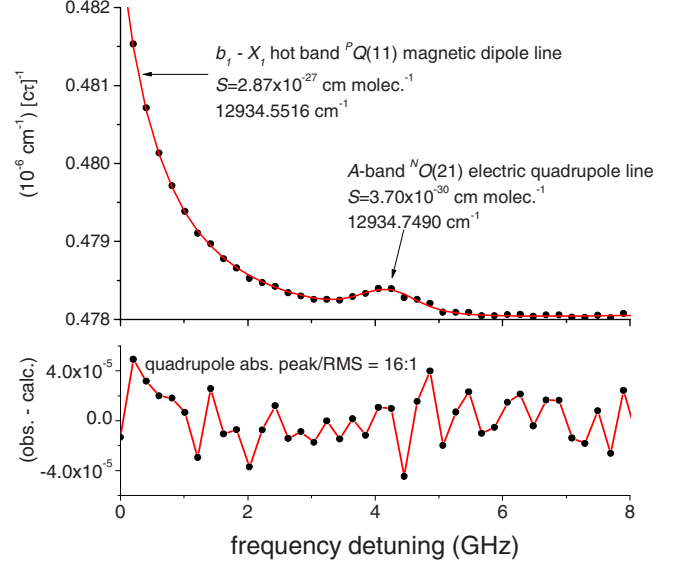

FIG. 10. (Color online) Upper panel gives the $^NO(21)$ electric quadrupole line ($\tilde{\nu} = 12\ 934.7490$ cm^{-1}, $S = 3.70 \times 10^{-30}$ cm molec.$^{-1}$) in the wings of the $^PQ(11)$ hot band, magnetic dipole transition of $^{16}O_2(\tilde{\nu} = 12\ 934.5516$ cm^{-1}, $S = 2.87 \times 10^{-27}$ cm molec.$^{-1}$). Symbols represent measured values and the lines are fitted Voigt line shapes. Bottom panel shows the fit residuals. The spectrum comprises an average of 23 files, taken at $p = 12.7$ kPa.

sured transitions are given in Table III. Since most measurements were made within 1 K of 296 K, the corrections required to adjust the measured intensities to T_r were all less than 0.7%, far below our experimental measurement uncertainty.

B. Uncertainty analysis

There are a number of observables in our experiment that do not make a significant contribution to the combined uncertainty in line intensity. These include measurements of the FSR, the spectrum frequency axis, and the sample temperature, pressure and number density. We estimate the relative combined uncertainty in S driven by uncertainties in these quantities to be less than 0.5%. There remain three dominant sources of uncertainty: (1) line shape effects influenced by collisional narrowing and self-broadening, (2) the base losses of the ring-down cavity, and (3) the total (base plus absorption) loss of the system. The first is a systematic (Type B) uncertainty, and the latter two can be treated as statistical uncertainties (Type A) that can be reduced by least-squares fits and signal averaging [48].

Our previous analysis of high SNR O_2 A band spectra [36] revealed collisional (Dicke) narrowing line shape effects which we modeled using the Galatry profile [43]. In the present study, we estimated that our choice of the Voigt profile contributes a relative uncertainty of <2% to S, with a larger uncertainty arising from our choice of broadening parameter. We found the systematic uncertainty in S arising from uncertainty in γ by numerical evaluation of the sensitivity parameter, $d \ln S/d \ln \gamma$. This parameter represents the

TABLE III. Measured electric quadrupole line intensities at 296 K (S in units of 10^{-30} cm molec.$^{-1}$), lower state energies (E'' in cm^{-1}) and standard relative uncertainties, [$u_{c,r}(S)$ in %] for the $^{16}O_2$ A band. The Type B uncertainties assume a 10% relative uncertainty in the self-broadening coefficient, γ. The quantities, n_T and $\langle n_s \rangle$ represent the number of measurements of S and the corresponding average number of co-added spectra, respectively.

Transition	E''	S	$u_{c,r}(S)$	Type A	Type B	n_T	$\langle n_s \rangle$
$^{N}O(5)$	42.2001	21.2	8.9	7.4	4.9	15	21
$^{N}O(13)$	260.6824	16.8	5.0	3.0	3.9	6	13
$^{N}O(15)$	343.9694	11.6	5.2	4.0	3.3	9	27
$^{N}O(17)$	438.7010	8.53	4.2	2.3	3.5	4	19
$^{N}O(19)$	544.8623	6.36	5.6	3.9	4.0	4	17
$^{N}O(21)$	662.4361	3.65	6.3	5.1	3.7	5	33
$^{P}O(1)$	2.0843	35.8	4.1	3.0	2.8	1	12
$^{R}S(1)$	0	3.83	11.0	9.9	4.7	1	45
$^{T}S(5)$	42.2240	20.5	4.4	3.0	3.3	1	10

fractional change in line intensity per fractional change in broadening parameter and can be readily found by repeating the fits to the quadrupole transitions over a range of γ values. From this analysis we obtain $d \ln S / d \ln \gamma \sim \eta p$, where η is line dependent and ranges from $(1.7-2.1)$ Pa^{-1}. Assuming a 10% relative uncertainty in γ, we find the relative uncertainty in S arising from error in γ to be less than 5% for all cases.

Variations in the base loss occurring on time scales that are comparable to the scan time can give rise to spurious structure in individual spectra. This type of effect may not be captured by a model that incorporates a simple linear or sinusoidal baseline. However, when taken over an ensemble of

FIG. 11. (Color online) Fit-derived peak areas (symbols), $\mathcal{A}_i$, vs O_2 number density, n, for the ^{N}O branch electric quadrupole lines given in Table II. The solid lines correspond to the expected areas based on the weighted mean line intensity for each case. The open symbols with abscissae near $n = 3.1 \times 10^{18}$ molec. cm^{-3}, are repeat measurements of the respective peak areas. The repeat data were obtained several weeks after the original data using another probe laser nominally identical to the original one.

spectra, residual variations in base losses tend to diminish inversely with the square root of the number of spectra, consistent with a Type A uncertainty. Likewise, noise in the ringdown signals occurring in the photoreceiver and A/D systems, limits the precision with which the ring-down time constant can be measured. This effect is manifest as an intrinsic noisiness in the spectra that is apparent near the detection limit. It too tends to be uncorrelated from one scan to the next, and hence both effects can be reduced by signal averaging as illustrated in Fig. 5.

The rms deviation in S about the ensemble mean $\langle S \rangle$ is a measure of the combined Type A uncertainty. For ^{N}O-branch lines (which are those for which several repeat measurements were made), Table III shows that this quantity ranges from 2.3% to 7.4%. We also repeated the peak area measurements as a further check on our measurement precision and reproducibility. These experiments were repeated for each line several weeks after the original data were taken (open symbols in Fig. 11), and data were acquired using a different probe laser that was nominally identical to the first. We found an average relative difference between the new S and those based on previously determined $\langle S \rangle$ of 1.3% with a standard deviation of 4.1%. These differences are consistent with the rms deviations in S that were found in the original data set.

Combining, the Type A and Type B uncertainties in quadrature, we estimate the relative combined standard uncertainty for most of the ^{N}O-branch electric quadrupole line intensities to be $\sim 6\%$. By comparison, this relative uncertainty is only about 20 times greater than those of the O_2 A band magnetic dipole lines [36]; despite the fact that the latter transitions are five orders of magnitude stronger than the former.

These data also indicate that it would be possible to detect much weaker lines using the present technique. Our weakest measured line had an intensity of 3.7×10^{-30} cm molec.$^{-1}$ with a Type A uncertainty of 5%. If we assume a best-case measurement precision of 2.5% (improved over the present case by a fourfold increase in signal averaging time or by a twofold reduction in mirror losses), we estimate a SNR of
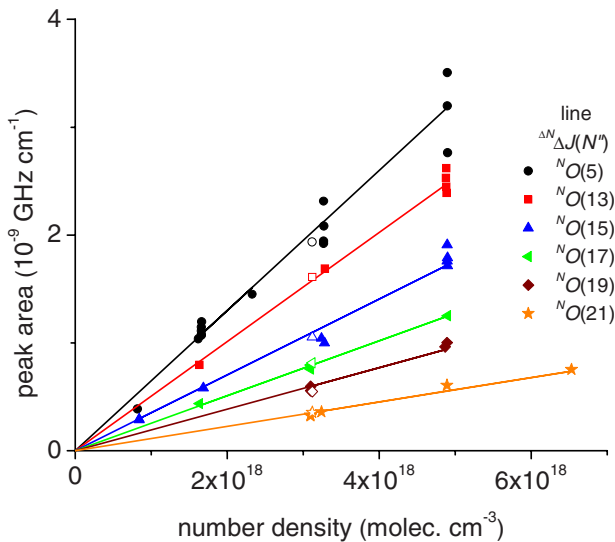
$\sim 2:1$ for a line having an intensity of 2×10^{-31} cm molec.$^{-1}$. This limit is approximately 100 times lower than the detection limit reported by Naus *et al.* [6] in their CRDS measurement of the $^{T}S(9)$ O_2 electric quadrupole line.

C. Electric quadrupole line intensity calculations

1. Transition quadrupole matrix elements

Intensities for quadrupole transitions have different frequency dependence than the more usual dipole transitions due to the extra length dimension of the quadrupole. Jackson [49] gives a thorough discussion of multipole electromagnetism. Using Eq. (16.97) of Jackson with wave number dimensions gives

$$R(\ell) = \overline{P_E(\ell)/P_E(1)} = \frac{9(\ell+1)}{2\ell[(2\ell+1)!!]^2}(2\pi\tilde{\nu})^{2(\ell-1)}\frac{|\overline{Q(\ell)}|^2}{|\overline{Q(1)}|^2}, \quad (3)$$

where $R(\ell)$ is the ratio of the average radiation of a multipole of order ℓ to the radiation of an electric dipole at wave number $\tilde{\nu}$. The other parts of Eq. (3) are

$$(2\ell+1)!! = (2\ell+1)(2\ell-1)\ldots 3, \quad (4)$$

$$\overline{P_E(\ell)} = \sum_m P_E(\ell,m), \quad (5)$$

$$|\overline{Q(\ell)}|^2 = \sum_m |Q(\ell,m)|^2. \quad (6)$$

The sum over m averages over the angular emission pattern so each multipole has spherical symmetry and there are no polarization effects. There are no cross terms between multipoles with different ℓ because of the orthogonality of the pattern for the fields. For a quadrupole ($\ell=2$),

$$R(2) = \frac{3}{100}(2\pi\tilde{\nu})^2\frac{|\overline{Q(2)}|^2}{|\overline{Q(1)}|^2}. \quad (7)$$

The matrix elements of the transition moments in Hund's case (b) can be derived using spherical tensor relations. The reduced matrix element for the transition moment is computed from the general equation for calculating the reduced matrix element in the space of J of a tensor product from reduced matrices for two tensors in the space of N and S (e.g., see Edmonds [50], Eq. 7.1.5)

$$\langle J_1,J_2,J||T^{(L)}||J_1',J_2',J'\rangle = \sqrt{(2J+1)(2J'+1)(2L+1)}$$
$$\times \begin{Bmatrix} J_1' & J_1 & L_1 \\ J_2' & J_2 & L_2 \\ J' & J & L \end{Bmatrix} \langle J_1||T^{(L_1)}||J_1'\rangle\langle J_2|$$
$$\times |T^{(L_2)}||J_2'\rangle, \quad (8)$$

where the quantity in brackets is a 9-J symbol. For coupling of N with S, $J_1=N$, $J_2=S$, and $L=L_J$. The tensor product is

TABLE IV. Operators satisfying triangular inequality found in Eq. (15).

L_J	L_S	L_N	$|\Delta N|$	Operator	Name
1	1	1	1	$[\hat{D}_0^1 \otimes S]^{(1)}$	M_1
2	1	1	1	$[\hat{D}_0^1 \otimes S]^{(2)}$	Q_1
2	1	3	1,3	$[\hat{D}_0^3 \otimes S]^{(2)}$	Q_3

$$T_J^{(L)} = [T_1^{(L_1)} \otimes T_2^{(L_2)}]^{(L)}. \quad (9)$$

In the present case, the generalized direction cosine operator, D_q^L, is an instance of $T_N^{(L_N)}$ with matrix elements given by

$$\langle N,K||D_q^{L_N}||N'K'\rangle = (-1)^{N-K}\sqrt{(2N+1)(2N'+1)}$$
$$\times \begin{pmatrix} N & L_N & N' \\ -K & q & K' \end{pmatrix}, \quad (10)$$

where the quantity in parentheses is a 3-J symbol. For Σ states with $K=K'=q=0$, the 3-J symbol is zero when $(N+N'+L_N)$ is odd. The three projections of $D_q^{(1)}$ with $q=0$, 1, and -1 are projections of a unit vector.

The choices for $T_S^{(L_S)}$ will be limited to $L_S=1$, where $T_S^{(1)}$ is the vector $\mathbf{S}$. The reduced matrix elements for singlet and triplet states are chosen by coupling two $S=1/2$ spins together using Eq. (8) with $J_1=J_2=1/2$, $L_1=L_2=L=1$.

$$\langle S||S||S'\rangle = \begin{bmatrix} 0 & \sqrt{3/8} \\ \sqrt{3/8} & \sqrt{3/2} \end{bmatrix}. \quad (11)$$

Note that $L_J=0$ for an operator that is part of the Hamiltonian, $L_J=1$ for an electric or magnetic dipole transition, and $L_J=2$ for a quadrupole transition. To include symmetry, we need to define a symmetrization of the direction cosine

$$\hat{D}_{q_N}^{L_N} = D_{q_N}^{L_N} + (-1)^{L_N+p_d}D_{-q_N}^{L_N} \quad (12)$$

For $K=K'=0$, the wave function is nonzero if $(p+N+s)$ is even. Here $s=1$ for a Σ^- state and $s=0$ for all other symmetries. Summing with a similar constraint for N' gives the requirement that

$$(p+p'+N+N'+s+s')\mathrm{mod}\,2 = 0. \quad (13)$$

Combining this expression with the constraint produced by the 3-J symbol in Eq. (10) gives

$$L_N\,\mathrm{mod}\,2 = (p+p'+s+s')\mathrm{mod}\,2. \quad (14)$$

The parity change, $(p+p')$, is even for magnetic dipoles and electric quadrupoles and odd for electric dipoles. Since the O_2 A band is $^1\Sigma_g^+ \leftarrow {}^3\Sigma_g^-$, L_N must be odd. The possible operators that satisfy the triangular inequality

$$|L_J - L_S| \leq L_N \leq L_J + L_S \quad (15)$$

are found in Table IV.

Therefore the A band intensities will depend on a single magnetic dipole, M_1, and two quadrupoles, Q_1 and Q_3. The relative sign of the quadrupoles can be determined using $\Delta N=1$ transitions, while $|Q_3|$ is largely determined using

ΔN=3 transitions. The intensities of the four electric quadrupole branches do not depend equally on Q_1 and Q_3. We expect that the Q_1 quadrupole dominates the $|\Delta N|$=1 transitions (>90% from Q_1 and ~10% Q_3), whereas the Q_3 quadrupole dominates the $|\Delta N|$=3 transitions (>95% from Q_3 and ≪10% from Q_1).

2. Fitted quadrupole moments

The SPCAT program [19] was modified to calculate the electric quadrupole matrix elements described above. Intensities for the $|\Delta N|$=1,3 electric quadrupole transitions were calculated for N''=1 to 29 (with estimated values for M_1, Q_1, and Q_3). The values of Q_1 and Q_3 were determined in a least-squares fit of the predicted electric quadrupole intensities to those we measured. A similar procedure was used to determine M_1 from the previously measured magnetic dipole transition intensities [36]. The fitted transition moments were: M_1=6.369(8)10^{-25} J T^{-1} [0.06868(8) Bohr-magnetons], Q_1=4.15(13)$\times 10^{-42}$ C m^2[0.0124(4) D Å], Q_3=2.61(8)$\times 10^{-42}$ C m^2[0.007 83(23) D Å], where the value in parentheses denotes the standard uncertainty in the last digit. We recalculated the predicted intensities for all four electric quadrupole branches using the fitted values of M_1, Q_1, and Q_3. The average absolute difference between the present electric quadrupole measurements and the calculations is ~5%, which is comparable to our reported average experimental uncertainty.

The results of these intensity calculations for all four electric quadrupole branches can be found in Table V. Figure 1 shows a stick spectrum based on the present calculations with all observed transitions indicated. Using the calculated transition moments, we calculated the transition band intensities: S_{MD}=2.25(2)$\times 10^{-22}$ cm molec.$^{-1}$ and S_{EQ}=1.8(1)$\times 10^{-27}$ cm molec.$^{-1}$. It is important to note that the $|\Delta N|$=1 transitions (i.e., ^PO and ^RS branches) are four times stronger than the $|\Delta N|$=3 transitions (i.e., ^NO and ^TS branches) as illustrated in Fig. 1, thus confirming the 1934 prediction of van Vleck [51]. As a result, while the ratio of intensities between a $|\Delta N|$=3 branch and a given magnetic dipole branch is 3×10^{-6} (as was reported by Brault [5]), the ratio of intensities for a $|\Delta N|$=1 electric quadrupole branch is 12×10^{-6}. After summing intensities over all branches, we find that the ratio of electric quadrupole and magnetic dipole band intensities is 8×10^{-6}.

On average, the measurements of Brault [5] are systematically low by 15% compared to the present calculations for the ^TS electric quadrupole transition intensities, displaying increasing discrepancy with large J. A deviation of ~12% was observed between Brault's $^TS(5)$ measurement and our own. These disparities are consistent with the quadrature sum of the 10% uncertainty in effective path length reported by Brault and the uncertainties in our calculations and measurements.

V. CONCLUSIONS

We have reported laboratory observations, quantitative intensity measurements, and calculations of electric quadru-

TABLE V. Calculated intensities (at 296 K, in units of 10^{-30} cm molec.$^{-1}$) for the electric quadrupole transitions within the ^NO, ^PO, ^RS, and ^TS branches of the $^{16}O_2$ A band. Fit uncertainties (mean absolute relative deviation between our measurements and calculated intensities) of these intensities are ~5%. Transitions observed in this study are underlined.

N''	^NO	^PO	^RS	^TS
1		35.9	4.09	6.09
3	11.4	76.5	51.2	14.0
5	18.7	102.3	80.9	19.8
7	21.8	114.0	96.6	22.7
9	21.9	112.3	98.9	22.8
11	19.7	100.4	90.9	20.7
13	16.3	82.4	76.2	17.2
15	12.5	62.7	58.8	13.2
17	8.83	44.4	42.1	9.46
19	5.86	29.4	28.2	6.32
21	3.62	18.2	17.6	3.95
23	2.11	10.6	10.3	2.31
25	1.15	5.78	5.68	1.27
27	0.60	2.97	2.93	0.661
29	0.29	1.44	1.42	0.318

pole transitions in the O_2 A band. These measurements may serve as a benchmark for ultrasensitive spectroscopic techniques. The experiment exploited the high sensitivity, spectral fidelity, and long-term stability of frequency-stabilized cavity ring-down spectroscopy; a technique that enabled intensity measurements of ultraweak lines ($S \sim 3 \times 10^{-30}$ to 2×10^{-29} cm molec.$^{-1}$) with unprecedented accuracy (4.4% to 11% relative combined uncertainty). Our calculations included the electric quadrupole line positions (uncertainties <3 MHz), matrix elements and line intensities. The line intensity calculations and measurements agreed to within our average experimental uncertainty of 6%. Our calculated positions and intensities are sufficiently accurate to model the electric quadrupole contribution to the O_2 A band which may be observed in long-path atmospheric spectra. In addition, we have demonstrated how such high-sensitivity and low-uncertainty measurements can add to our understanding of diatomic spectroscopy and provide a basis for comparison with present day computational models. Finally, the measurements of other ultraweak transitions in atmospherically relevant species may have possible future implications for increasingly sensitive remote sensing measurements.

[1] J. F. Noxon, Can. J. Phys. **39**, 1110 (1961).

[2] A. Goldman, J. Reid, and L. S. Rothman, Geophys. Res. Lett. **8**, 77 (1981).

[3] E. Niple, W. G. Mankin, A. Goldman, D. G. Murcray, and F. J. Murcray, Geophys. Res. Lett. **7**, 489 (1980).

[4] J. Reid, R. L. Sinclair, A. M. Robinson, and A. R. W. McKellar, Phys. Rev. A **24**, 1944 (1981).

[5] J. W. Brault, J. Mol. Spectrosc. **80**, 384 (1980).

[6] H. Naus, A. deLange, and W. Ubachs, Phys. Rev. A **56**, 4755 (1997).

[7] D. M. O'Brien, S. A. English, and G. DaCosta, J. Atmos. Ocean. Technol. **14**, 105 (1997).

[8] R. A. Washenfelder, G. C. Toon, J. F. Blavier, Z. Yang, N. T. Allen, P. O. Wennberg, S. A. Vay, D. M. Matross, and B. C. Daube, J. Geophys. Res., [Atmos.] **111**, D22305 (2006).

[9] K. Chance, J. Quant. Spectrosc. Radiat. Transf. **58**, 375 (1997).

[10] S. Corradini and M. Cervino, J. Quant. Spectrosc. Radiat. Transf. **97**, 354 (2006).

[11] B. van Diedenhoven, O. P. Hasekamp, and I. Aben, Atmos. Chem. Phys. **5**, 2109 (2005).

[12] M. Yokomizo, Fujitsu Sci. Tech. J. **44**, 410 (2008).

[13] D. Crisp, R. M. Atlas, F. M. Breon *et al.* in *Trace Constituents in the Troposphere and Lower Stratosphere* (Pergamon-Elsevier Science Ltd, Kidlington, 2004) Vol. 34, p. 700.

[14] C. E. Miller, L. R. Brown, R. A. Toth, D. C. Benner, and V. M. Devi, C. R. Phys. **6**, 876 (2005).

[15] C. E. Miller, D. Crisp, P. L. DeCola *et al.*, J. Geophys. Res., [Atmos.] **112**, D10314 (2007).

[16] C. E. Miller and D. Wunch (unpublished).

[17] H. D. Babcock and L. Herzberg, Astrophys. J. **108**, 167 (1948).

[18] H. Lefebvre-Brion and R. W. Field, *The Spectra and Dynamics of Diatomic Molecules* (Elsevier, New York, 2004).

[19] H. M. Pickett, J. Mol. Spectrosc. **148**, 371 (1991).

[20] M. Yu. Tretyakov, M. A. Koshelev, V. V. Dorovskikh, D. S. Makarov, and P. W. Rosenkranz, J. Mol. Spectrosc. **231**, 1 (2005).

[21] G. Y. Golubiatnikov and A. F. Krupnov, J. Mol. Spectrosc. **217**, 282 (2003).

[22] Y. Endo and M. Mizushima, Jpn. J. Appl. Phys., Part 2 **21**, L379 (1982).

[23] K. Park, I. G. Nolt, T. C. Steele, L. R. Zink, K. M. Evenson, K. V. Chance, and A. G. Murray, J. Quant. Spectrosc. Radiat. Transf. **56**, 315 (1996).

[24] L. R. Zink and M. Mizushima, J. Mol. Spectrosc. **125**, 154 (1987).

[25] G. Rouillé, G. Millot, R. Saint-Loup, and H. Berger, J. Mol. Spectrosc. **154**, 372 (1992).

[26] G. Millot, B. Lavorel, and G. Fanjoux, J. Mol. Spectrosc. **176**, 211 (1996).

[27] S. Brodersen and J. Bendtsen, J. Mol. Spectrosc. **219**, 248 (2003).

[28] K. W. Brown, N. H. Rich, and J. W. Nibler, J. Mol. Spectrosc. **151**, 482 (1992).

[29] D. J. Robichaud, J. T. Hodges, P. Masłowski, L. Y. Yeung, M. Okumura, C. E. Miller, and L. R. Brown, J. Mol. Spectrosc. **251**, 27 (2008).

[30] L. R. Brown and C. Plymate, J. Mol. Spectrosc. **199**, 166 (2000).

[31] A. J. Phillips, F. Peters, and P. A. Hamilton, J. Mol. Spectrosc. **184**, 162 (1997).

[32] R. Schermaul and R. C. M. Learner, J. Quant. Spectrosc. Radiat. Transf. **61**, 781 (1999).

[33] D. J. Robichaud, J. T. Hodges, D. Lisak, C. E. Miller, and M. Okumura, J. Quant. Spectrosc. Radiat. Transf. **109**, 435 (2008).

[34] J. T. Hodges, H. P. Layer, W. W. Miller, and G. E. Scace, Rev. Sci. Instrum. **75**, 849 (2004).

[35] J. T. Hodges and R. Ciuryło, Rev. Sci. Instrum. **76**, 023112 (2005).

[36] D. J. Robichaud, J. T. Hodges, L. R. Brown, D. Lisak, P. Masłowski, L. Y. Yeung, M. Okumura, and C. E. Miller, J. Mol. Spectrosc. **248**, 1 (2008).

[37] D. J. Robichaud, L. Y. Yeung, D. A. Long, M. Okumura, D. K. Havey, J. T. Hodges, C. E. Miller, and L. R. Brown, J. Phys. Chem. A (to be published).

[38] D. Halmer, G. von Basum, P. Hering, and M. Murtz, Rev. Sci. Instrum. **75**, 2187 (2004).

[39] D. W. Allan, Proc. IEEE **54**, 221 (1966).

[40] P. Werle, R. Mücke, and F. Slemr, Appl. Phys. B: Lasers Opt. **57**, 131 (1993).

[41] D. Romanini and K. K. Lehmann, J. Chem. Phys. **99**, 6287 (1993).

[42] S. Kassi, D. Romanini, A. Campargue, and B. Bussery-Honvault, Chem. Phys. Lett. **409**, 281 (2005).

[43] L. Galatry, Phys. Rev. **122**, 1218 (1961).

[44] P. L. Varghese and R. K. Hanson, Appl. Opt. **23**, 2376 (1984).

[45] P. R. Berman, J. Quant. Spectrosc. Radiat. Transf. **12**, 1331 (1972).

[46] Z. Yang, P. O. Wennberg, R. P. Cageao, T. J. Pongetti, G. C. Toon, and S. P. Sander, J. Quant. Spectrosc. Radiat. Transf. **90**, 309 (2005).

[47] L. S. Rothman, I. E. Gordon, A. Barbe *et al.*, J. Quant. Spectrosc. Radiat. Transf. **110**, 533 (2009).

[48] B. N. Taylor and C. E. Kuyatt, NIST Tech. Note **1297** (1994).

[49] J. D. Jackson, *Classical Electrodynamics* (John Wiley, New York, 1962), pp. 538–577.

[50] A. R. Edmonds, *Angular Momentum in Quantum Mechanics* (Princeton University Press, Princeton, New Jersey, 1974).

[51] J. H. van Vleck, Astrophys. J. **80**, 161 (1934).